Fast and Accurate Algorithm for the Short-Pulse Electromagnetic Scattering From Conducting Circular Plates Buried Inside a Lossy Dispersive Half-Space

Vicente Losada, Rafael R. Boix, *Member, IEEE*, and Francisco Medina, *Senior Member, IEEE*

***Abstract*—The method of moments in the Hankel transform domain is applied to the determination of the fields scattered by a conducting circular plate buried in a lossy dispersive half-space when the plate is illuminated by a plane wave. The scattered fields obtained in the frequency domain are used to model the time-domain short-pulse scattering via the inverse fast Fourier transform. The authors show that the choice of adequate basis functions in the approximation of the current density induced on the plate makes it possible to obtain very accurate results for the scattered fields while using low computer memory requirements and short CPU times. This implies that the algorithm developed for the particular problem treated in this paper provides a good benchmark for the validation of any other numerical algorithms dealing with the analysis of the scattering from buried conducting objects with more complex geometry.**

***Index Terms*—Buried objects, electromagnetic (EM) scattering, fast algorithm, method of moments.**

I. Introduction

GROUND-PENETRATING radar (GPR) using electromagnetic waves is an important tool for the detection and identification of buried objects with military applications [detection of mines or unexploded ordnance (UXO)] as well as civilian applications (detection of conduits) [1]–[3]. In relation to this topic, in the last few years many researchers have been working in the development of numerical algorithms for the analysis of the electromagnetic scattering by buried conducting and dielectric objects both in the frequency domain [3]–[8] and in the time domain [9]–[15]. The scattering by buried objects has been studied by different numerical methods such as the finite element method (FEM) [3], finite differences in time domain (FDTD) [9], [14], the method of moments (MoM) [4]–[7], [10]–[13], [15], and the conjugate gradient method combined with fast Fourier transform (CG-FFT) [8]. Among all these numerical methods, the MoM is the method most frequently used.

In the particular case of the scattering by buried planar conducting objects, little work has been carried out as mentioned in [15]. As far as the authors know, all the results published in the literature refer to buried planar conducting objects of rectangular geometry [4]–[8], [15]. In this paper, the authors apply the MoM in the frequency domain to the analysis of the scattering by a circular conducting plate buried in a lossy dispersive half-space. Also, the results obtained in the frequency domain are used for modeling the time-domain short-pulse scattering from the circular plate by means of the inverse FFT as in [10]–[13] and [15]. In the study carried out, the revolution axis of the circular plate is assumed to be normal to the air–ground interface (i.e., the plate is treated as a body of revolution (BOR) in the sense cited in [11] and [12]), which makes it possible to compute the entries of the MoM matrix in the Hankel transform domain (HTD) as in [16]. Special home-made basis functions are used for approximating the current density on the plate so that the basis functions provide a quick convergence of the MoM with respect to the number of basis functions. Also, asymptotic extraction techniques are used for the fast evaluation of the infinite integrals arising from the application of the MoM in the HTD [16]. As a result of these two latter facts, the algorithm developed for the analysis of the scattering of buried circular conducting plates in the frequency and time domains turns out to be a very accurate and fast tool. The results obtained with this tool can be used as a reliable benchmark for the validation of other numerical algorithms devoted to the analysis of the scattering from buried conducting objects.

The remainder of the text is organized as follows. In Section II of the paper, the authors describe the application of the MoM in the HTD to the determination of the fields scattered by the buried circular plate under plane wave illumination, and the subsequent use of the results obtained for computing the time-domain short-pulse scattering. In Section III, the validity of the algorithm developed is checked by comparing our results with published results for the far fields scattered by a circular plate in free space [17], [18]. Good agreement is found among the two sets of results. Also, in Section III, original results are presented for the fields scattered by a circular plate buried in a dispersive lossy half-space both in the frequency domain and in the time domain.

II. Problem Geometry and Numerical Procedure

Fig. 1 shows the side view of a circular conducting plate of radius a buried in a lossy dispersive half-space. The circular plate is assumed to be a perfect electric conductor (PEC) of negligible thickness, and the revolution axis of the plate is taken to

Manuscript received June 17, 2002; revised December 10, 2002. This work was supported by the Spanish Comisión Interministerial de Ciencia y Tecnología and European Union funds (FEDER) under Project TIC2001–3163.

V. Losada is with the Department of Applied Physics I, Microwaves Group, School of Agricultural Engineering, University of Seville, 41013, Seville, Spain.

R. R. Boix and F. Medina are with the Department of Electronics and Electromagnetism, Microwaves Group, School of Physics, University of Seville, 41012 Seville, Spain (e-mail:boix@us.es).

Digital Object Identifier 10.1109/TGRS.2003.810678

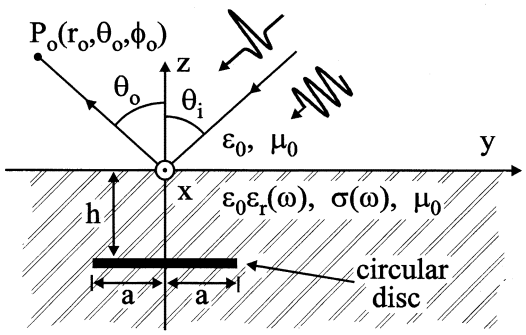

Fig. 1. Side view of a circular conducting plate buried in a lossy dispersive half-space. The circular plate is illuminated by either a time-harmonic plane wave or a short-pulse plane wave. The direction of propagation of the plane waves makes an angle θ_i with the z axis. $P_o(r_o, \theta_o, \phi_o)$ is the point chosen for the observation of the scattered fields.

be normal to the interface between the air and the lossy medium (i.e., the circular plate is assumed to be a BOR in the sense of [11]). The lossy half-space is assumed to be made of a nonmagnetic material ($\mu_r = 1$) with frequency-dependent permittivity $\epsilon_0\epsilon_r(\omega)$ and conductivity $\sigma(\omega)$.

A. MoM in the HTD for the Computation of the Scattered Fields in the Frequency Domain

Consider a time-harmonic TEM plane wave traveling through the air upper half-space of Fig. 1 with direction of propagation characterized by the unit vector $\hat{\boldsymbol{u}}_i = -(\cos\phi_i \sin\theta_i \hat{\boldsymbol{x}} + \sin\phi_i \sin\theta_i \hat{\boldsymbol{y}} + \cos\theta_i \hat{\boldsymbol{z}})$. When this plane wave impinges on the interface between the air and the lossy medium, a reflected wave arises in the air half-space, a damped transmitted wave arises in the lossy half-space, and finally, a scattered wave arises in both half-spaces owing to the current induced in the circular conducting plate by the transmitted wave. The electromagnetic fields related to all these waves will be assumed to have a time dependence of the type $e^{j\omega t}$, which will be suppressed all along this subsection. Let $\mathbf{E}_{ap}(x, y, z; \omega)$ be the electric field generated in the two half-spaces of Fig. 1 by the incident plane wave when the circular plate is absent. In the presence of the circular plate, the total electric field generated by the incident plane will be the sum of $\mathbf{E}_{ap}(x, y, z; \omega)$ and the scattered electric field. If we force that the tangential component of this total electric field on the circular plate is zero, we obtain an electric field integral equation (EFIE) for the induced current on the plate, $\mathbf{j}(x, y; \omega)$. This EFIE can be written as shown at the bottom of the page where $\overline{\mathbf{G}}_t(x - x', y - y', z \mid z'; \omega)$ is a 2×2 matrix that stands for the transverse (to z) dyadic Green's function (see [19, eq. (10)]) of the two half-spaces medium of Fig. 1. The vector function $\mathbf{E}_{ap}(x, y, z = -h; \omega)$ appearing in (1) can be explicitly written in terms of x and y as

$$\mathbf{E}_{ap}(x, y, z = -h; \omega) = (E_{0x}(\omega)\hat{\boldsymbol{x}} + E_{0y}(\omega)\hat{\boldsymbol{y}} + E_{0z}(\omega)\hat{\boldsymbol{z}}) \cdot e^{jk_0(\sin\theta_i \cos\phi_i x + \sin\theta_i \sin\phi_i y)} \quad (2)$$

where $k_0 = \omega\epsilon_0\mu_0$, and the quantities $E_{0s}(\omega)$ ($s = x, y, z$) can be obtained in closed form after a trivial calculation.

In order to solve the EFIE of (1), in the current paper the authors have expressed the unknown current density on the circular plate in cylindrical coordinates $\mathbf{j}(\rho, \phi; \omega)$ as a Fourier series of the cylindrical coordinate ϕ (see [11, eq. (15)])

$$\mathbf{j}(\rho, \phi; \omega) = \sum_{m=-\infty}^{+\infty} \mathbf{j}_m(\rho; \omega) e^{jm\phi}. \quad (3)$$

Then, the vector functions $\mathbf{j}_m(\rho; \omega)$ ($m = \ldots, -1, 0, 1, \ldots$) of (3) [which appear in the modal decomposition of $\mathbf{j}(\rho, \phi; \omega)$] have been approximated as linear combinations of known basis functions $\mathbf{j}_i^m(\rho)$ ($i = 0, \ldots, 2M$; $m = \ldots, -1, 0, 1, \ldots$) as

$$\mathbf{j}_m(\rho; \omega) = \sum_{i=0}^{2M} a_i^m(\omega)\mathbf{j}_i^m(\rho), \ (m = \ldots, -1, 0, 1, \ldots). \quad (4)$$

With a view to obtaining the unknown coefficients $a_i^m(\omega)$ ($i = 0, \ldots, 2M$; $m = \ldots, -1, 0, 1, \ldots$), (3) and (4) have been introduced in (1), and the Galerkin's version of the MoM has been applied to the resulting expression. The final product of these operations has turned out to be a system of infinite linear equations for $a_i^m(\omega)$ (in practice, this system of equations has a finite number of unknowns since a finite number of terms can only be retained in the series of (3) in the numerical computations). Once Galerkin's method has been applied to the EFIE of (1), the entries of Galerkin's matrix have been expressed as double infinite integrals in the two-dimensional (2-D) Fourier transform domain (2-D–FT) by means of Parseval's theorem. This step is very convenient and is based on the fact that whereas the transverse dyadic Green's function of (1) $\overline{\mathbf{G}}_t(x - x', y - y', z \mid z')$ cannot be obtained in closed form in the spatial domain, its 2-D–FT (see [19, eq. (11)]) can be obtained in a straightforward way [19]. After expressing the entries of Galerkin's matrix in the 2-D–FT domain, a further step has been to introduce polar spectral variables in the determination of these entries (as in [16]) so as to take advantage of the revolution symmetry of the structure of Fig. 1 around the z axis. This latter step has made it possible to express the entries of Galerkin's matrix as single infinite integrals in the Hankel transform domain (HTD) [16]. As a result of all the aforementioned operations, the original system of infinite linear equations for the unknowns $a_i^m(\omega)$ ($i = 0, \ldots, 2M$ $m = \ldots, -1, 0, 1, \ldots$) has been transformed into a set of decoupled finite systems of linear equations in such a way that all the unknowns sharing the

$$\hat{\boldsymbol{z}} \times \left[\mathbf{E}_{ap}(x, y, z = -h; \omega) + \int\int_{x'^2 + y'^2 \le a^2} \overline{\mathbf{G}}_t(x - x', y - y', z = -h \mid z' = -h; \omega) \cdot \mathbf{j}(x', y'; \omega) dx' dy' \right] = \mathbf{0}, \quad x^2 + y^2 \le a^2 \quad (1)$$

same value of the Fourier mode integer m in (4) only appear in one system of equations (just as in [11, eq. (19)]). The resulting system of equations for the mth Fourier mode can be written as

$$\sum_{i=0}^{2M} \Gamma_{ji}^{m}(\omega) a_i^m(\omega) = b_j^m(\omega), \quad (j = 0\ldots, 2M;\ m = \ldots, -1, 0, 1, \ldots) \quad (5)$$

where the expression of the coefficients $\Gamma_{ji}^{m}(\omega)$ and $b_j^m(\omega)$ in the HTD is given by (6), shown at the bottom of the page, and by

$$b_i^m(\omega) = -\left[\left(\widetilde{\mathbf{j}}_i^{H(m)}(k_\rho = k_0 \sin\theta_i)\right)^*\right]^t \cdot \begin{pmatrix} E_{0x}(\omega) + jE_{0y}(\omega) \\ E_{0x}(\omega) - jE_{0y}(\omega) \end{pmatrix}, \quad (i = 0\ldots, 2M;\ m = \ldots, -1, 0, 1, \ldots). \quad (7)$$

The 2×2 matrix $\widetilde{\overline{\mathbf{G}}}_t^H(k_\rho, z = -h \mid z' = -h; \omega)$ of (6) is the transverse dyadic Green's function in the HTD defined in [16, eq. (14)] (source and field points at the plane of the circular plate). This matrix can be obtained in closed form for the particular case of the two half-spaces medium of Fig. 1 as shown in the Appendix . Concerning the vector functions in the HTD $\widetilde{\mathbf{j}}_i^{H(m)}(k_\rho)$ $(i = 0, \ldots, 2M; m = \ldots, -1, 0, 1, \ldots)$ appearing in (6) and (7), these functions can be obtained in terms of the Hankel transforms of the basis functions $\mathbf{j}_i^m(\rho)$ of (4) as

$$\widetilde{\mathbf{j}}_i^{H(m)}(k_\rho) = \int_0^\infty \begin{bmatrix} \left(j_{i,\rho}^m(\rho) + jj_{i,\phi}^m(\rho)\right) J_{m+1}(k_\rho \rho) \\ \left(j_{i,\rho}^m(\rho) - jj_{i,\phi}^m(\rho)\right) J_{m-1}(k_\rho \rho) \end{bmatrix} \rho d\rho, \quad (i = 0\ldots, 2M;\ m = \ldots, -1, 0, 1, \ldots). \quad (8)$$

The infinite integrals of (6) have to be computed along an integration path C located in the first quadrant of the complex k_ρ plane above the two branch points and the poles of $\widetilde{\overline{\mathbf{G}}}_t^H(k_\rho, z = -h \mid z' = -h; \omega)$ [16], [20]. It should be pointed out that the method used in this paper for studying the scattering by the circular plate of Fig. 1 can be easily extended to deal with the scattering of a circular plate embedded in a multilayered lossy medium of the type cited in [12] and [20]. In the latter case, the study just requires the use of (6) in the expression of $\widetilde{\overline{\mathbf{G}}}_t^H(k_\rho, z = -h \mid z' = -h; \omega)$ that is valid for a multilayered medium, which can be obtained by means of a recurrent algorithm based on the equivalent boundary method [16], [21].

Once the unknown coefficients $a_i^m(\omega)$ are determined for a certain choice of the basis functions $\mathbf{j}_i^m(\rho)$ of (4), it is possible to compute the scattered electric field. In particular, the application of the stationary phase method (see [22, pp. 164–169]) makes it possible to obtain an expression for the far-zone electric field scattered by the circular plate of Fig. 1 in the air half-space $\mathbf{E}_{ff}^{sc}(r, \theta, \phi; \omega)$ $(\theta \leq \pi/2)$. This expression is given by (9), shown at the bottom of the page, where the functions in the HTD $\widetilde{E}_+^{H(m)}(k_\rho; \omega)$ and $\widetilde{E}_-^{H(m)}(k_\rho; \omega)$ can be obtained as

$$\begin{pmatrix} \widetilde{E}_+^{H(m)}(k_\rho; \omega) \\ \widetilde{E}_-^{H(m)}(k_\rho; \omega) \end{pmatrix} = \sum_{i=0}^{2M} a_i^m(\omega) \widetilde{\overline{\mathbf{G}}}_t^H(k_\rho, z = 0 \mid z' = -h; \omega) \cdot \widetilde{\mathbf{j}}_i^{H(m)}(k_\rho), \quad (m = \ldots, -1, 0, 1, \ldots). \quad (10)$$

The Appendix describes how to obtain $\widetilde{\overline{\mathbf{G}}}_t^H(k_\rho, z = 0 \mid z' = -h; \omega)$, which stands for the transverse dyadic Green's function in the HTD when the source point is at the plane of the circular plate of Fig. 1 and the field point is at the interface between the air and the lossy medium.

If we establish an observation direction in the air half-space of Fig. 1 characterized by the unit vector $\hat{\boldsymbol{u}}_o = \cos\phi_o \sin\theta_o \hat{\boldsymbol{x}} + \sin\phi_o \sin\theta_o \hat{\boldsymbol{y}} + \cos\theta_o \hat{\boldsymbol{z}}$ $(\theta_o \leq \pi/2)$, the different components of the bistatic radar cross section (RCS) matrix of the buried circular plate can be computed in terms of $\mathbf{E}_{ff}^{sc}$

$$\sigma_{uv}(\theta_o, \phi_o, \theta_i, \phi_i; \omega) = \frac{4\pi r^2 |\mathbf{E}_{ff}^{sc}(r, \theta = \theta_o, \phi = \phi_o; \omega) \cdot \hat{\boldsymbol{v}}|^2}{|E_u^i|^2}, \quad (u, v = \theta, \phi) \quad (11)$$

where $\mathbf{E}_{sc}^{ff} \cdot \hat{\boldsymbol{v}}$ stands for the v component of the scattered far field $(v = \theta, \phi)$, and $|E_u^i|$ stands for the magnitude of the electric field of an incident plane wave polarized in the u direction $(u = \theta, \phi)$.

Although some GPR systems work in the far zone of the targets [1], [2], some others measure the scattered fields at the

$$\Gamma_{ji}^{m}(\omega) = \int_{0(C)}^{\infty} \left[\left(\widetilde{\mathbf{j}}_j^{H(m)}\left(k_\rho^*\right)\right)^*\right]^t \cdot \widetilde{\overline{\mathbf{G}}}_t^H(k_\rho, z = -h \mid z' = -h; \omega) \cdot \widetilde{\mathbf{j}}_i^{H(m)}(k_\rho) k_\rho dk_\rho, \quad (i, j = 0, \ldots, 2M;\ m = \ldots, -1, 0, 1, \ldots) \quad (6)$$

$$\mathbf{E}_{ff}^{sc}(r, \theta, \phi; \omega) = \frac{k_0 e^{-jk_0 r}}{2r} \left\{ j\hat{\boldsymbol{\theta}} \sum_{m=-\infty}^{+\infty} e^{j(m+1)\pi/2} e^{jm\phi} \cdot \left[\widetilde{E}_+^{H(m)}(k_\rho = k_0 \sin\theta; \omega) - \widetilde{E}_-^{H(m)}(k_\rho = k_0 \sin\theta; \omega)\right] + \hat{\boldsymbol{\phi}} \cos\theta \sum_{m=-\infty}^{+\infty} e^{j(m+1)\pi/2} e^{jm\phi} \cdot \left[\widetilde{E}_+^{H(m)}(k_\rho = k_0 \sin\theta; \omega) + \widetilde{E}_-^{H(m)}(k_\rho = k_0 \sin\theta; \omega)\right] \right\} \quad (9)$$

air–ground interface [11]. This indicates that it is not only interesting to compute the fields scattered by the circular plate of Fig. 1 in the far zone but also in the zone of the air half-space closest to the buried plate. Since the scattered electric field in this latter zone cannot be obtained by means of (9), it is necessary to develop expressions for the scattered electric field which are valid at any point of the air half-space. These expressions can be obtained in cylindrical coordinates in the HTD, as in (12)–(14), shown at the bottom of the page, where $\widetilde{E}_{+}^{H(m)}(k_\rho;\omega)$ and $\widetilde{E}_{-}^{H(m)}(k_\rho;\omega)$ have been defined in (10).

Concerning the choice of the basis functions of (4), $\mathbf{j}_i^m(\rho)$ ($i = 0,\ldots,2M$; $m = \ldots,-1,0,1,\ldots$), we have taken into account that the scattering response of a buried target is strongly related to its natural resonances [15]. Bearing in mind this idea, the basis functions have been chosen to be very similar to those used in the approximation of the current density on a circular microstrip patch while studying the resonant modes of the patch [16]. The following basis functions are used in this paper:

$$\mathbf{j}_i^0(\rho) = j\frac{T_{2i}\left(\frac{\rho}{a}\right)}{\sqrt{1-\left(\frac{\rho}{a}\right)^2}}\left(\frac{\rho}{a}\right)\hat{\boldsymbol{\phi}}, \qquad (i=0,\ldots,M) \tag{15}$$

$$\mathbf{j}_i^0(\rho) = U_{2i-2M-1}\left(\frac{\rho}{a}\right)\sqrt{1-\left(\frac{\rho}{a}\right)^2}\hat{\boldsymbol{\rho}}, \qquad (i=M+1,\ldots,2M) \tag{16}$$

$$\mathbf{j}_i^m(\rho) = j\frac{T_{2i}\left(\frac{\rho}{a}\right)}{\sqrt{1-\left(\frac{\rho}{a}\right)^2}}\left(\frac{\rho}{a}\right)^{|m|-1}\hat{\boldsymbol{\phi}}, \qquad (i=0,\ldots,M;\ m=\ldots,-1,1,\ldots) \tag{17}$$

$$\mathbf{j}_i^m(\rho) = U_{2i-2M-1}\left(\frac{\rho}{a}\right)\sqrt{1-\left(\frac{\rho}{a}\right)^2}\left(\frac{\rho}{a}\right)^{|m|-2}\hat{\boldsymbol{\rho}}, \qquad (i=M+1,\ldots,2M;\ m=\ldots,-1,1,\ldots). \tag{18}$$

The basis functions of (15)–(18) have several advantages. First, they accurately reproduce the expected physical behavior of the current density around the center ($\rho \to 0$) and the edge ($\rho \to a$) of the buried circular plate for each Fourier mode of (3) [16], which ensures a quick convergence of the scattered field results with respect to the number of basis functions when MoM is applied (see Section III for more details). Second, their Hankel transforms can be obtained in closed form in terms of spherical Bessel functions (see [16, App. B]), and this makes very efficient the numerical implementation of Galerkin's method in the HTD. And finally, these basis functions lead to infinite integrals of the type shown in (8) which are amenable to asymptotic analytical integration techniques (see [16, Sec. IV and App. C]), and these integration techniques introduce important CPU time savings in the numerical computation of the aforementioned infinite integrals.

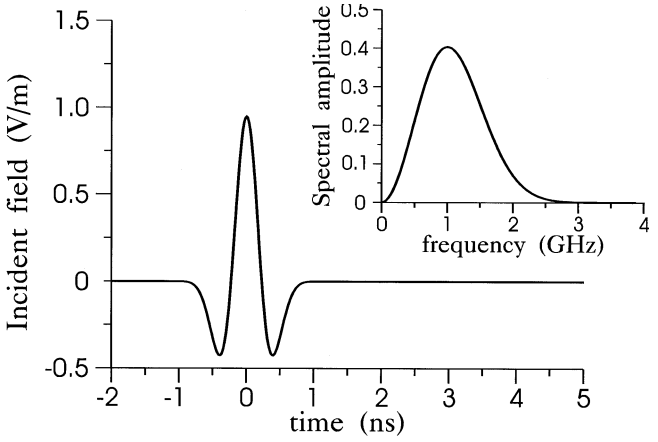

Fig. 2. Incident time-domain short pulse used in the numerical calculations and its spectrum.

B. Computation of the Scattered Fields in the Time Domain

In order to perform the scattering analysis in the time domain, an ultrawideband short-pulse plane wave with direction of propagation characterized by the unit vector $\hat{\boldsymbol{u}}_i$ is assumed to impinge on the interface between the air and the lossy medium. The time dependence of the short pulse and its spectrum are shown in Fig. 2. The spectrum contains frequencies up to approximately 3 GHz (center frequency is around 1 GHz), and its mathematical expression is given by

$$F(\omega) = 1.5\tau_2\sqrt{2\pi}e^{-\omega^2\tau_2^2/2}e^{-2(\pi\tau_2/\tau_1)^2} \cdot\left[\cosh\left(\frac{2\pi\omega\tau_2^2}{\tau_1}\right)-1\right] \tag{19}$$

where $\tau_1 = 1.2$ ns and $\tau_2 = 0.27$ ns. Once the scattered fields have been computed in the frequency domain, the time-domain scattered fields can be obtained via inverse Fourier transform.

$$E_\rho^{sc}(\rho,\phi,z\geq 0;\omega) = \frac{1}{2}\sum_{m=-\infty}^{+\infty} e^{jm\phi}\int_{0(C)}^{\infty}\left[\widetilde{E}_{+}^{H(m)}(k_\rho;\omega)J_{m+1}(k_\rho\rho)+\widetilde{E}_{-}^{H(m)}(k_\rho;\omega)J_{m-1}(k_\rho\rho)\right]e^{-z\sqrt{k_\rho^2-k_0^2}}\,k_\rho dk_\rho \tag{12}$$

$$E_\phi^{sc}(\rho,\phi,z\geq 0;\omega) = \frac{1}{2j}\sum_{m=-\infty}^{+\infty} e^{jm\phi}\int_{0(C)}^{\infty}\left[\widetilde{E}_{+}^{H(m)}(k_\rho;\omega)J_{m+1}(k_\rho\rho)-\widetilde{E}_{-}^{H(m)}(k_\rho;\omega)J_{m-1}(k_\rho\rho)\right]e^{-z\sqrt{k_\rho^2-k_0^2}}\,k_\rho dk_\rho \tag{13}$$

$$E_z^{sc}(\rho,\phi,z\geq 0;\omega) = \frac{1}{2}\sum_{m=-\infty}^{+\infty} e^{jm\phi}\int_{0(C)}^{\infty}J_m(k_\rho\rho)\left[\widetilde{E}_{+}^{H(m)}(k_\rho;\omega)-\widetilde{E}_{-}^{H(m)}(k_\rho;\omega)\right]\frac{e^{-z\sqrt{k_\rho^2-k_0^2}}}{\sqrt{k_\rho^2-k_0^2}}\,k_\rho^2 dk_\rho \tag{14}$$

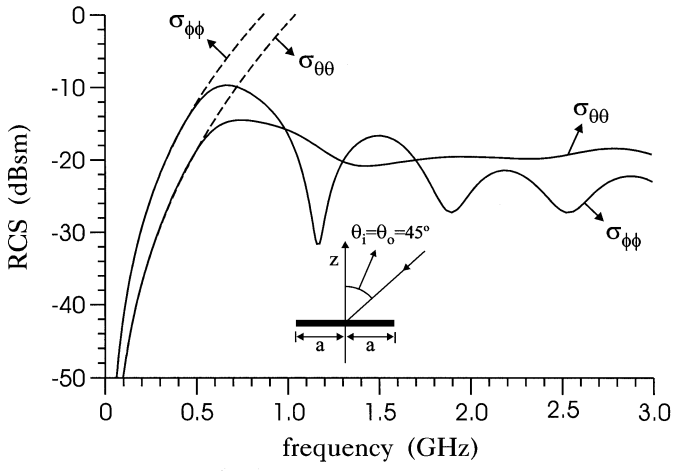

Fig. 3. Monostatic RCS components $\sigma_{\theta\theta}$ and $\sigma_{\phi\phi}$ of a conducting circular plate in free space ($a = 100$ mm) versus frequency. Our MoM results (solid lines) are compared with the results obtained by means of the low-frequency formulae of [17] (dashed lines).

In particular, the time-domain far-zone scattered electric field $\mathbf{E}_{ff}^{sc}(r,\theta,\phi;t)$ can be obtained in terms of its frequency domain equivalent of (9), $\mathbf{E}_{ff}^{sc}(r,\theta,\phi;\omega)$, as

$$\mathbf{E}_{ff}^{sc}(r,\theta,\phi;t) = \frac{1}{2\pi}\int_{-\infty}^{\infty} \mathbf{E}_{ff}^{sc}(r,\theta,\phi;\omega)F(\omega)e^{j\omega t}d\omega. \quad (20)$$

Expressions similar to (20) can be derived for the determination of the components of the time-domain near-zone scattered electric field in terms of their frequency domain equivalents of (12)–(14).

The time-domain scattered field results appearing in Section III of the current paper have been generated by means of the FFT algorithm, and 1024 frequency points have always been used as in [10]. Also, once the observation point of spherical coordinates $P_o(r_o,\theta_o,\phi_o)$ has been fixed (see Fig. 1), in the results of Section III the time origin has been deliberately shifted and chosen to be the instant at which the peak of the incident short pulse passes through the point of spherical coordinates (r_o,θ_i,ϕ_i).

III. Numerical Results

In order to check the validity of the algorithm described in Section II, in Figs. 3 and 4 our numerical results for the RCS of a perfectly conducting circular plate in free space are compared with published results obtained via application of the T-matrix method [17], [18]. In Fig. 3, our results are compared with those arising from the low-frequency closed-form expressions of the scattered far-fields derived in [17, eqs. (4.18.a) and (4.18.b)] by means of the T-matrix method. These low-frequency expressions contain the exact first three terms in the power-series expansions of the scattered far-fields in k_0a. Note that our results match those provided by the low-frequency expressions of [17] up to 0.5 GHz (i.e., up to $k_0a \approx 1$) for incident waves with both parallel and perpendicular polarizations. In Fig. 4(a) and (b), our results for the RCS are compared with the T-matrix results published in [18, Figs. 7.b and 10.b]. Despite the fact that in this latter case $k_0a \approx 8.5$, the agreement between our set of results

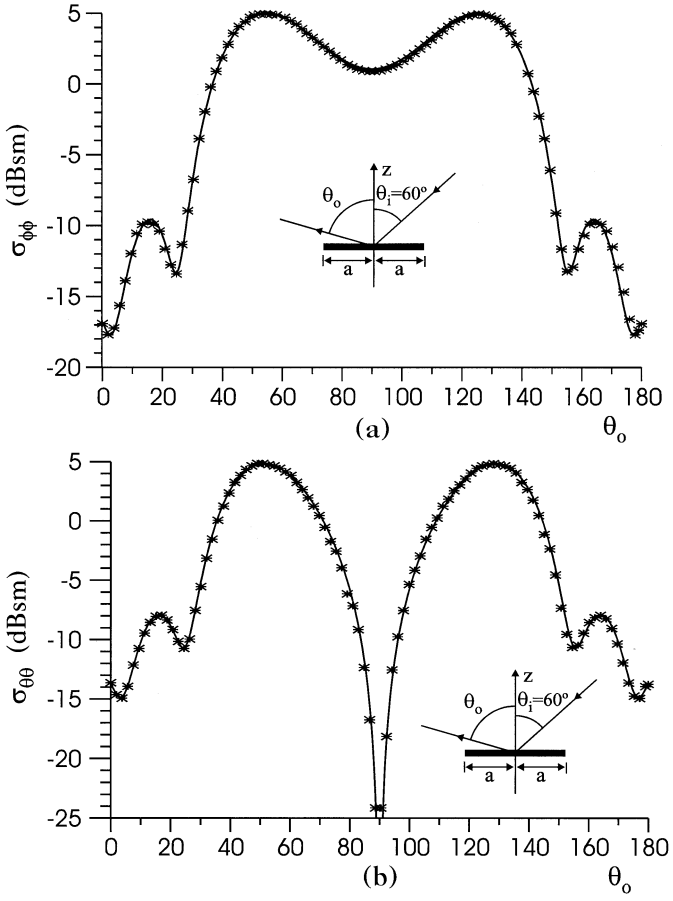

Fig. 4. Bistatic RCS components (a) $\sigma_{\phi\phi}$ and (b) $\sigma_{\theta\theta}$ of a conducting circular plate in free space ($a = 100$ mm, $f = 2$ GHz, $\phi_i = 0°$, $\phi_o = 180°$) versus the observation angle θ_o. Our MoM results (solid lines) are compared with results obtained by means of the T-matrix method [18] ($*$).

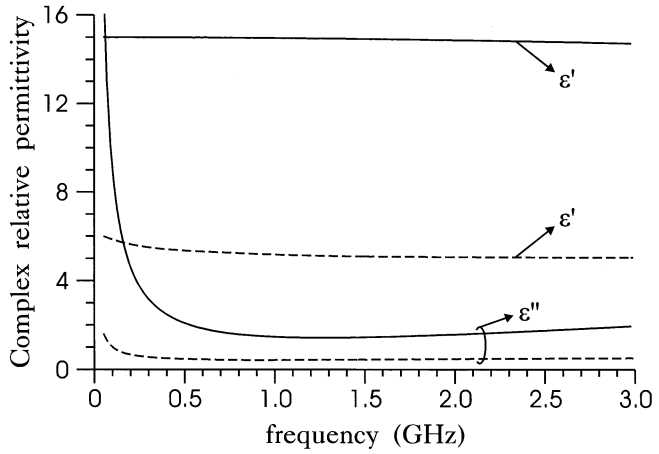

Fig. 5. Complex relative permittivities $\epsilon' - j\epsilon''$ of wet soil (with about 20% water content) reported in [14] (solid lines) and Puerto Rico clay (with 10% water content) reported in [23] (dashed lines). The relative permittivity of the wet soil is modeled by means of the Debye formula [14] ($\epsilon_{rs} = 15$, $\epsilon_{r\infty} = 5$, $\sigma_0 = 0.05$ S/m, $\tau = 9 \cdot 10^{-12}$ s), and that of Puerto Rico clay is derived from measurements published in [23].

and the set of T-matrix results of [18] is still excellent for the two types of polarizations studied.

In Fig. 5, the authors plot the real and imaginary parts of the complex relative permittivity of the two lossy dispersive

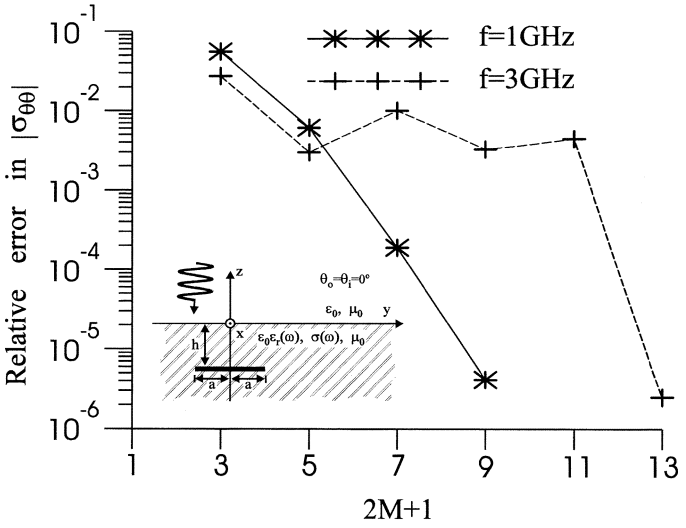

Fig. 6. Relative error in the monostatic RCS component $\sigma_{\theta\theta}$ of a conducting circular plate buried in Puerto Rico clay (see Fig. 5) versus the number of basis functions used in (4) ($a = 100$ mm, $h = 100$ mm). Normal incidence is considered ($\theta_i = \theta_o = 0°$). The errors in the values of $\sigma_{\theta\theta}(2M+1)$ were computed with respect to $\sigma_{\theta\theta}(2M+1=11)$ when $f = 1$ GHz, and with respect to $\sigma_{\theta\theta}(2M+1=15)$ when $f = 3$ GHz.

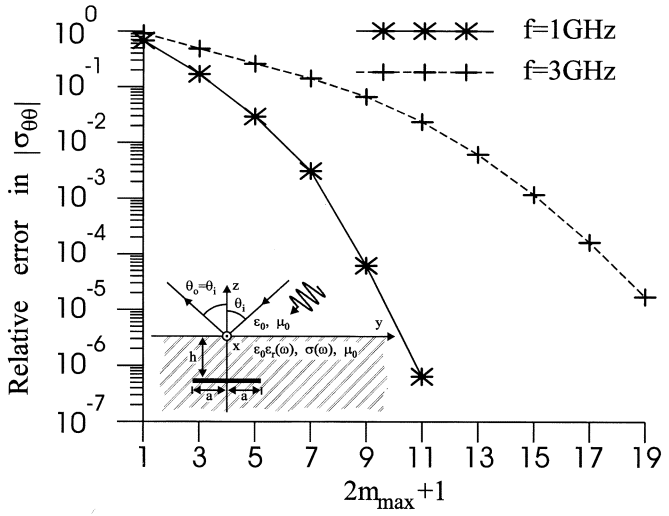

Fig. 7. Relative error in the bistatic RCS component $\sigma_{\theta\theta}$ of a conducting circular plate buried in Puerto Rico clay versus the total number of Fourier modes retained in (3) when $-m_{\max} \leq m \leq m_{\max}$ ($a = 100$ mm, $h = 100$ mm). Oblique incidence is considered ($\theta_i = 66.1°$, $\phi_i = 0°$), and the observation is carried out in the reflection direction ($\theta_o = 66.1°$, $\phi_o = 180°$). The errors in the values of $\sigma_{\theta\theta}(2m_{\max}+1)$ were computed with respect to $\sigma_{\theta\theta}(2m_{\max}+1=13)$ when $f = 1$GHz, and with respect to $\sigma_{\theta\theta}(2m_{\max}+1=21)$ when $f = 3$ GHz. $2M+1=9$ is used in all cases.

materials used throughout this section for occupying the lower half-space of Fig. 1. The first material is wet soil (with about 20% water content) for which the frequency-dependent relative permittivity and conductivity are modeled via the Debye formula as shown in [14, eqs. (1) and (2) and Table 1]. The second material is Puerto Rico clay (with 10% water content) for which the authors use the measured values of the relative permittivity and conductivity that are published in [23] (as in [10]–[12] and [20]). Note that both the relative permittivity and the conductivity of the Debye wet soil are roughly three times larger than those of Puerto Rico clay.

In Fig. 6, the relative error made in the computation of the RCS of a circular plate embedded in Puerto Rico clay (see Fig. 5) is plotted as a function of the number of basis functions used in the approximation of the current density. The incident plane wave impinges normally on the air–soil interface (i.e., $\theta_i = 0°$ in Fig. 1), and it can be proved that for this particular case (normal incidence), only the Fourier modes $m = -1$ and $m = +1$ take part in the expansion (3) of the induced current density. That means that the number $2M+1$ of Fig. 6 strictly refers to the basis functions of (17) and (18) for $m = \pm 1$. Despite of the fact that convergence in the values of $|\sigma_{\theta\theta}|$ is reached in Fig. 6 for both $f = 1$GHz and $f = 3$ GHz, whereas convergence is nearly exponential when $f = 1$ GHz, the convergence turns oscillatory and requires a larger number of basis functions when $f = 3$ GHz. In fact, whereas seven basis functions suffice to provide convergence within four significant figures when $f = 1$GHz, an accuracy of four significant figures is not reached until $2M+1 = 13$ when $f = 3$ GHz. In order to explain why more basis functions are required in the approximation of the current density as the frequency increases, one should think that the dependence of the current density with the radial cylindrical coordinate ρ becomes more complex with increasing frequency. Fig. 7 shows results for the RCS of a circular plate buried in Puerto Rico clay when the incident plane wave impinges obliquely on the air–soil interface, which implies that no Fourier modes can be discarded *a priori* in the expansion (3) of the current density. In Fig. 7, the authors plot the relative error in the RCS values as a function of the total number of Fourier modes retained in (3), $2m_{\max}+1$ (more precisely, the Fourier modes retained are those located between $m = -m_{\max}$ and $m = m_{\max}$). Note that convergence with respect to $2m_{\max}+1$ is faster for lower frequencies. Thus, whereas nine Fourier modes suffice to achieve convergence within four significant figures when $f = 1$ GHz, 17 Fourier modes are necessary for providing a similar accuracy when $f = 3$ GHz. As it happens with the number of basis functions, the reason why more Fourier modes are required in (3) as the frequency increases is that the dependence of the current density on the azimuthal cylindrical coordinate ϕ becomes more complex with increasing frequency. This close relation between the number of Fourier modes retained in (3) and frequency has been reported in [12]. One of the most important conclusions that can be drawn from Figs. 6 and 7 is that extremely accurate results can be obtained for the RCS of the buried circular plate of Fig. 1 with a few basis functions of the type shown in (15)–(18). This indicates that the mentioned basis functions are very appropriate for approximating the surface current density induced on the circular plate by an incident plane wave.

In Fig. 8, the bistatic RCS of a circular plate buried in Puerto Rico clay is plotted versus frequency for different plate depths. The incidence angle θ_i has been chosen to be the Brewster angle of a lossless half-space with relative permittivity equal to that of Puerto Rico clay at $f = 1.5$ GHz. Note that the effect of losses on the RCS values begins to be important for depths around 300 mm, and especially for frequencies larger than 1 GHz (in fact, Fig. 8 shows that beyond this frequency, the RCS values for $h = 300$ mm quickly decrease far below -30 dBsm). Note that the RCS values of the buried plate show oscillations which are

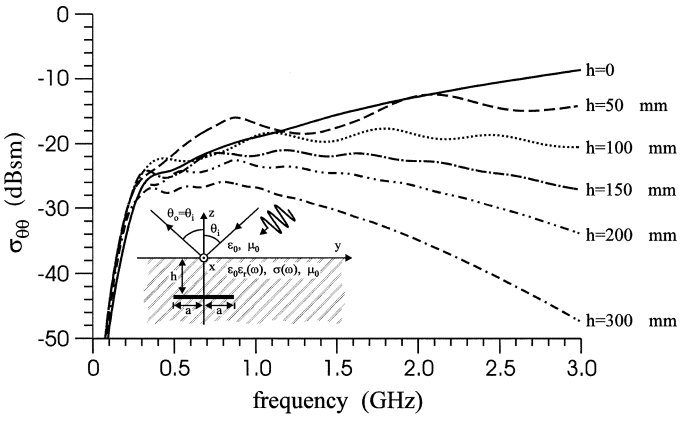

Fig. 8. Bistatic RCS component $\sigma_{\theta\theta}$ of a conducting circular plate buried in Puerto Rico clay (see Fig. 5) for different plate depths ($a = 100$ mm, $\theta_i = 66.1°$, $\phi_i = 0°$). Observation is carried out in the reflection direction ($\theta_o = 66.1°$, $\phi_o = 180°$).

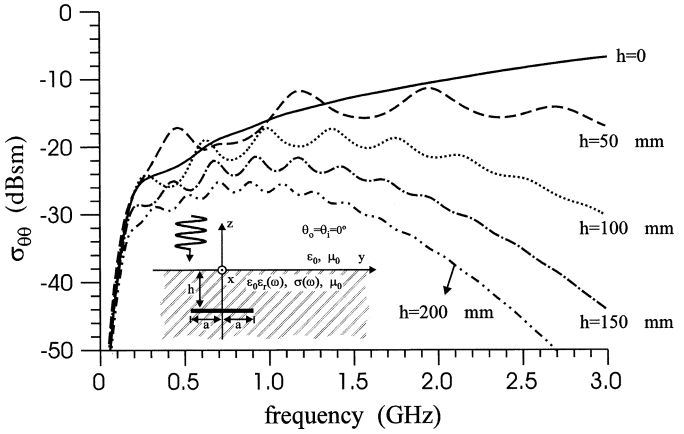

Fig. 9. Monostatic RCS component $\sigma_{\theta\theta}$ of a conducting circular plate buried in Debye wet soil (see Fig. 5) for different plate depths ($a = 100$ mm). Normal incidence is considered ($\theta_i = \theta_o = 0°$).

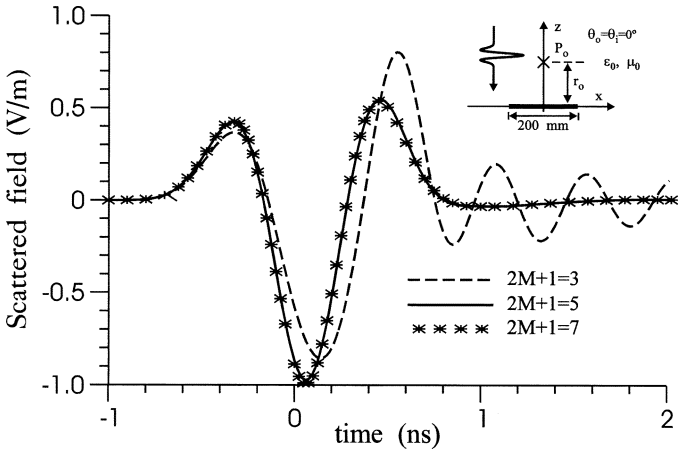

Fig. 10. Time-domain fields backscattered by a conducting circular plate in free space ($a = 100$ mm). Normal incidence is considered ($\theta_i = \theta_o = 0°$), and the observation point is located a distance $r_o = 10$ mm above the circular plate center. Convergence with respect to the number of basis functions used in (4) is studied.

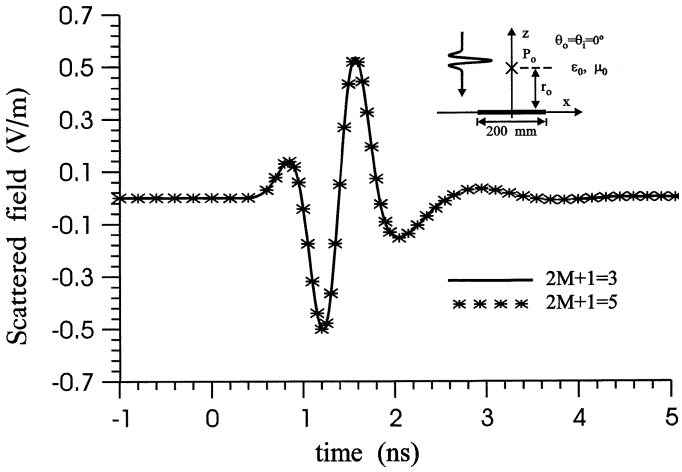

Fig. 11. Time-domain fields backscattered by a conducting circular plate in free space ($a = 100$ mm). Normal incidence is considered ($\theta_i = \theta_o = 0°$), and the observation point is located a distance $r_o = 200$ mm above the circular plate center. Convergence with respect to the number of basis functions used in (4) is studied.

not present when the plate is placed at the air–soil interface (case $h = 0$). These oscillations show resonant peaks which periodically appear every time the depth roughly increases one-half wavelength in the soil region, which is in agreement with the theory exposed in [24]. Fig. 9 shows results for the monostatic RCS of a circular plate buried in Debye wet soil (see Fig. 5) under normal incidence conditions. If Figs. 8 and 9 are compared, one observes that the RCS values of a plate placed at the air–soil interface are of the same order for all frequencies. However, since Debye wet soil losses are larger than Puerto Rico clay losses, the RCS values of a circular plate buried in Debye wet soil tend to be smaller than those of a circular plate buried in Puerto Rico clay at the same depth, the differences between the two set of RCS values being more relevant as the depth increases. Note that for plates buried at the same depth, the period of the RCS oscillations are smaller in Fig. 9 than in Fig. 8, which is due to the fact that the relative permittivity of Debye wet soil is larger than that of Puerto Rico clay (and therefore, the wavelength at the same frequency is smaller).

Figs. 10 and 11 show results for the fields backscattered by a conducting circular plate in free space when the short pulse of Fig. 2 normally impinges on the plate. Whereas in Fig. 10 the observation point is chosen to be a distance from the plate center much smaller than the plate radius, in Fig. 11 the observation point is chosen to be a distance from the plate center equal to the plate diameter. Both Figs. 10 and 11 show the convergence of the scattered fields with respect to the number of basis functions used in (4). The convergence of the scattered fields is reached in visual form when only five basis functions are used in the case of Fig. 10, and when three basis functions are used in the case of Fig. 11. This indicates that the basis functions of (15)–(18) not only provide a quick convergence of the results in the frequency domain (see Figs. 6 and 7) but also in the time domain. Note that the number of basis functions required to achieve convergence is larger in Fig. 10 than in Fig. 11. This is attributed to the fact that the accurate computation of the scattered fields requires a more and more accurate determination of the induced current density as we move closer to the plate surface. The shape of the scattered

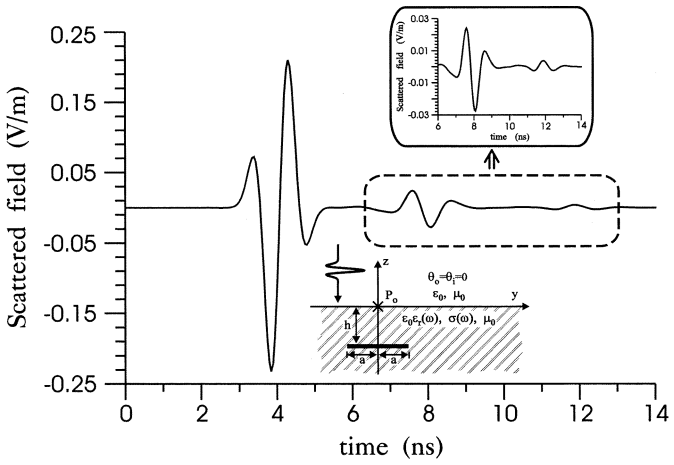

Fig. 12. Time-domain fields backscattered by a conducting circular plate buried in Debye wet soil ($a = 100$ mm, $h = 150$ mm). Normal incidence is considered ($\theta_i = \theta_o = 0°$), and the observation point is located at the air–soil interface above the circular plate center ($r_o = 0$).

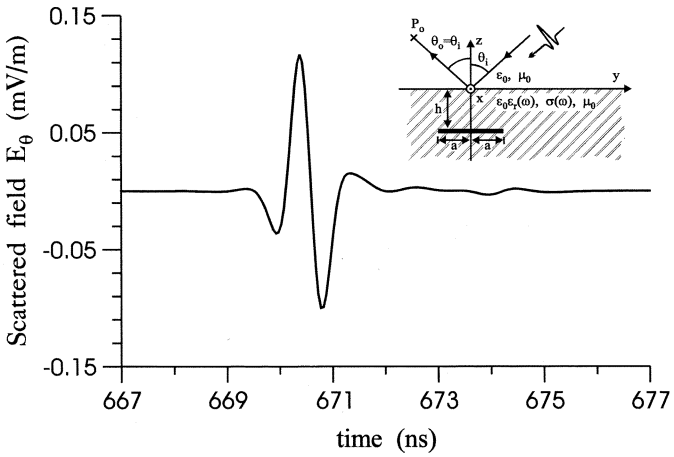

Fig. 13. Time-domain fields scattered by a conducting circular plate buried in Puerto Rico clay ($a = 100$ mm, $h = 250$ mm). Oblique incidence is considered ($\theta_i = 66.1°$, $\phi_i = 0°$), and the observation point is assumed to be placed in the air region far–zone along the reflection direction ($r_o = 100$ m, $\theta_0 = 66.1°$, $\phi_o = 180°$). The incident pulse is polarized along the $\hat{\boldsymbol{\theta}}$ direction.

pulse of Fig. 10 is basically that of the pulse of Fig. 2 with the sign changed, which indicates that the circular plate roughly behaves as an infinite conducting plane at the observation point of Fig. 10. However, the shape of the scattered pulse of Fig. 11 strongly differs from the shape of the pulse of Fig. 2, which shows that the effect of the finite size of the plate on the scattered pulse is noticeable at the observation point of Fig. 11.

Fig. 12 considers short-pulse scattering from a conducting circular plate buried in Debye wet soil. The observation point is assumed to be placed at the air–soil interface above the center of the circular plate. The scattered fields show a first return from the circular plate centered around 4 ns, which is roughly the time that the short pulse takes to go from the observation point to the plate and come back. Also, there is a weaker second return around 8 ns and a much weaker third return around 12 ns (noticeable in the detail of Fig. 12), which are attributed to reverberations between the air–soil interface and the circular plate. Note that the shape of the first return closely resembles that of the scattered pulse of Fig. 11. Also, the shape of the second return is similar to that of the first return with the sign changed. In Fig. 13, results are presented for the short-pulse scattering from a conducting circular plate buried in Puerto Rico clay. Oblique incidence is assumed in this case. Whereas the scattered fields of Figs. 10–12 have been obtained in terms of the time-domain version of the exact expressions (12) and (13), in Fig. 13 the time-domain scattered fields have been computed in the far zone via the asymptotic expressions (9) and (20). In this latter figure, there is a first return from the circular plate around 670.5 ns, which is roughly the time that the pulse of Fig. 2 takes to go from the point of spherical coordinates (r_o, θ_i, ϕ_i) to the circular plate plus the time that the scattered pulse takes to go from the circular plate to the observation point. There is also a much weaker second return around 674 ns, which corresponds to an oblique reverberation between the air–soil interface and the circular plate.

It should be pointed out that the CPU time required to obtain the curve of Fig. 12 was roughly 4 min on a 300-MHz PC (with the code written in Fortran 77), and the CPU time required for the curve of Fig. 13 was roughly 7 min. These CPU times could have been considerably diminished if the elements of the MoM matrix had been interpolated as a function of frequency as commented in [10], but interpolation was not carried out. The authors of [11] and [12] said that they needed hours of CPU time (in personal computers similar to that employed by the authors of the current paper) for the computation of the time-domain fields scattered by conducting bodies of revolution, despite the fact they interpolated the MoM matrix. This shows that the algorithm described in Section II for the particular problem solved in this paper is not only accurate (as demonstrated in Figs. 6, 7, 10, and 11) but also extremely fast by comparison with previously developed algorithms for the study of related problems.

IV. Conclusion

The MoM in the HTD has been applied to the analysis of the electromagnetic scattering from a conducting circular plate buried in a lossy dispersive half-space. The results obtained in the frequency domain have been used for modeling the time-domain short-pulse scattering from the circular plate by means of the inverse FFT. The use of adequate basis functions in the approximation of the current density on the plate has made it possible to develop an algorithm which provides very accurate results for the scattered fields while using low computer memory requirements and short CPU times. This algorithm can be used as a reliable benchmark for the validation of other numerical algorithms devoted to the analysis of the scattering from buried conducting objects. The algorithm has been checked by comparing our results with published results for the RCS of circular plates in free space. Good agreement has been found between the two sets of results. Some original results have been presented for the RCS of circular plates buried in realistic lossy dispersive soils. These RCS results tend to oscillate with increasing frequency, and quickly decrease as the plates depth increases. Also, some new results have been presented for the short-pulse scattering from buried circular plates. These results clearly show the first echo from the circular plate and subsequent reverberations between the air–soil interface and the circular plate.

APPENDIX

In order to obtain the expressions of the two matrices

$$\widetilde{\widetilde{\mathbf{G}}}_t^H(k_\rho, z=-h \mid z'=-h;\omega)$$

[see (6)] and

$$\widetilde{\widetilde{\mathbf{G}}}_t^H(k_\rho, z=0 \mid z'=-h;\omega)$$

[see (10)] for the two half-spaces medium of Fig. 1, let us define first the three matrices $\widetilde{\widetilde{\mathbf{A}}}$, $\widetilde{\widetilde{\mathbf{B}}}$, and $\widetilde{\widetilde{\mathbf{C}}}$ given by

$$\widetilde{\widetilde{\mathbf{A}}} = -j\left[\coth(\tilde{\beta}_r h)+1\right]\widetilde{\widetilde{\mathbf{W}}}_r \tag{21}$$

$$\widetilde{\widetilde{\mathbf{B}}} = \frac{j}{\sinh(\tilde{\beta}_r h)}\widetilde{\widetilde{\mathbf{W}}}_r \tag{22}$$

$$\widetilde{\widetilde{\mathbf{C}}} = -j\left[\widetilde{\widetilde{\mathbf{W}}}_0 + \coth(\tilde{\beta}_r h)\widetilde{\widetilde{\mathbf{W}}}_r\right] \tag{23}$$

where

$$\widetilde{\widetilde{\mathbf{W}}}_r = \frac{j}{2}\begin{pmatrix} \left(\frac{\omega\epsilon_0\epsilon_r - j\sigma}{\tilde{\beta}_r} - \frac{\tilde{\beta}_r}{\omega\mu_0}\right) & -\left(\frac{\omega\epsilon_0\epsilon_r - j\sigma}{\tilde{\beta}_r} + \frac{\tilde{\beta}_r}{\omega\mu_0}\right) \\ -\left(\frac{\omega\epsilon_0\epsilon_r - j\sigma}{\tilde{\beta}_r} + \frac{\tilde{\beta}_r}{\omega\mu_0}\right) & \left(\frac{\omega\epsilon_0\epsilon_r - j\sigma}{\tilde{\beta}_r} - \frac{\tilde{\beta}_r}{\omega\mu_0}\right) \end{pmatrix} \tag{24}$$

$$\widetilde{\widetilde{\mathbf{W}}}_0 = \frac{j}{2}\begin{pmatrix} \left(\frac{\omega\epsilon_0}{\tilde{\beta}_0} - \frac{\tilde{\beta}_0}{\omega\mu_0}\right) & -\left(\frac{\omega\epsilon_0}{\tilde{\beta}_0} + \frac{\tilde{\beta}_0}{\omega\mu_0}\right) \\ -\left(\frac{\omega\epsilon_0}{\tilde{\beta}_0} + \frac{\tilde{\beta}_0}{\omega\mu_0}\right) & \left(\frac{\omega\epsilon_0}{\tilde{\beta}_0} - \frac{\tilde{\beta}_0}{\omega\mu_0}\right) \end{pmatrix} \tag{25}$$

and

$$\tilde{\beta}_r = \sqrt{k_\rho^2 - k_0^2\epsilon_r + j\omega\mu_0\sigma} \tag{26}$$

$$\tilde{\beta}_0 = \sqrt{k_\rho^2 - k_0^2}. \tag{27}$$

Then, $\widetilde{\widetilde{\mathbf{G}}}_t^H(k_\rho, z=-h \mid z'=-h;\omega)$ and $\widetilde{\widetilde{\mathbf{G}}}_t^H(k_\rho, z=0 \mid z'=-h;\omega)$ can be obtained in terms of $\widetilde{\widetilde{\mathbf{A}}}$, $\widetilde{\widetilde{\mathbf{B}}}$, and $\widetilde{\widetilde{\mathbf{C}}}$ as

$$\widetilde{\widetilde{\mathbf{G}}}_t^H(k_\rho, z=-h \mid z'=-h;\omega) = \left(\widetilde{\widetilde{\mathbf{A}}} - \widetilde{\widetilde{\mathbf{B}}}\cdot\widetilde{\widetilde{\mathbf{C}}}^{-1}\cdot\widetilde{\widetilde{\mathbf{B}}}\right)^{-1} \tag{28}$$

$$\widetilde{\widetilde{\mathbf{G}}}_t^H(k_\rho, z=0 \mid z'=-h;\omega) = \left(\widetilde{\widetilde{\mathbf{B}}} - \widetilde{\widetilde{\mathbf{A}}}\cdot\widetilde{\widetilde{\mathbf{B}}}^{-1}\cdot\widetilde{\widetilde{\mathbf{C}}}\right)^{-1} \tag{29}$$

REFERENCES

[1] S. Vitebskiy, L. Carin, M. A. Ressler, and F. H. Le, "Ultra-wideband, short-pulse, ground-penetrating radar: Simulation and measurement," *IEEE Trans. Geosci. Remote Sensing*, vol. 35, pp. 762–772, May 1997.

[2] L. Carin, N. Geng, M. Mclure, J. Sichina, and L. Nguyen, "Ultra-wide band synthetic-aperture radar for mine-field detection," *IEEE Antennas Propagat. Mag.*, vol. 41, pp. 18–33, Feb. 1999.

[3] K. O'Neill, S. A. Haider, S. D. Geimer, and K. D. Paulsen, "Effects of the ground surface on polarimetric features of broadband radar scattering from subsurface metallic objects," *IEEE Trans. Geosci. Remote Sensing*, vol. 39, pp. 1556–1565, July 2001.

[4] K. A. Michalski and D. Zheng, "Electromagnetic scattering and radiation by surfaces of arbitrary shape in layered media, Part II: Implementation and results for contiguous half-spaces," *IEEE Trans. Antennas Propagat.*, vol. 38, pp. 345–352, Mar. 1990.

[5] J. Chen, A. A. Kishk, and A. W. Glisson, "MPIE for conducting sheets penetrating a multilayer medium," in *Proc. IEEE Antennas Propagat. Symp. Dig.*, 1994, pp. 1346–1349.

[6] T. J. Cui, W. Wiesbeck, and A. Herschlein, "Electromagnetic scattering by multiple three-dimensional scatterers buried under multilayered media-Part II: Numerical implementations and results," *IEEE Trans. Geosci. Remote Sensing*, vol. 36, pp. 535–546, Mar. 1998.

[7] T. J. Cui and W. C. Chew, "Fast evaluation of sommerfeld integrals for EM scattering and radiation by three-dimensional buried objects," *IEEE Trans. Geosci. Remote Sensing*, vol. 37, pp. 887–900, Mar. 1999.

[8] ——, "Fast algorithm for electromagnetic scattering by buried conducting plates of large size," *IEEE Trans. Antennas Propagat.*, vol. 47, pp. 1116–1118, June 1999.

[9] K. Demarest, R. Plumb, and Z. Huang, "FDTD modeling of scatterers in stratified media," *IEEE Trans. Antennas Propagat.*, vol. 43, pp. 1164–1168, Oct. 1995.

[10] S. Vitebskiy and L. Carin, "Moment-method modeling of short-pulse scattering from and the resonances of a wire buried inside a lossy, dispersive half-space," *IEEE Trans. Antennas Propagat.*, vol. 43, pp. 1303–1312, Nov. 1995.

[11] S. Vitebskiy, K. Sturgess, and L. Carin, "Short-pulse plane-wave scattering from buried perfectly conducting bodies of revolution," *IEEE Trans. Antennas Propagat.*, vol. 44, pp. 143–151, Feb. 1996.

[12] N. Geng and L. Carin, "Wide-band electromagnetic scattering from a dielectric BOR buried in a layered lossy dispersive medium," *IEEE Trans. Antennas Propagat.*, vol. 47, pp. 610–619, Apr. 1999.

[13] ——, "Short-pulse electromagnetic scattering from arbitrarily oriented subsurface ordnance," *IEEE Trans. Geosci. Remote Sensing*, vol. 37, pp. 2111–2113, July 1999.

[14] T. P. Montoya and G. S. Smith, "Land mine detection using a ground-penetrating radar based on resistively loaded vee dipoles," *IEEE Trans. Antennas Propagat.*, vol. 47, pp. 1795–1806, Dec. 1999.

[15] Y. Wang, I. D. Longstaff, C. J. Leat, and N. V. Shuley, *IEEE Trans. Geosci. Remote Sensing*, vol. 39, pp. 1183–1189, June 2001.

[16] V. Losada, R. R. Boix, and M. Horno, "Resonant modes of circular microstrip patches in multilayered substrates," *IEEE Trans. Microwave Theory Tech.*, vol. 47, pp. 488–498, Apr. 1999.

[17] G. Kristensson and P. C. Waterman, "The T matrix for acoustic and electromagnetic scattering by circular disks," *J. Acoust. Soc. Amer.*, vol. 72, no. 5, pp. 1612–1625, Nov. 1982.

[18] T. Martin, "An improved near- to far-zone transformation for the finite-difference time-domain method," *IEEE Trans. Antennas Propagat.*, vol. 46, pp. 1263–1271, Sept. 1998.

[19] R. R. Boix, N. G. Alexopoulos, and M. Horno, "Efficient numerical computation of the spectral transverse dyadic Green's function in stratified anisotropic media," *J. Electromagn. Waves Appl.*, vol. 10, no. 8, pp. 1047–1083, 1996.

[20] N. Geng, D. R. Jackson, and L. Carin, "On the resonances of a dielectric BOR buried in a dispersive layered medium," *IEEE Trans. Antennas Propagat.*, vol. 47, pp. 1305–1313, Aug. 1999.

[21] F. L. Mesa, R. Marques, and M. Horno, "A general algorithm for computing the bidimensional spectral Green's dyad in multilayered complex bianisotropic media: The equivalent boundary method," *IEEE Trans. Microwave Theory Tech.*, vol. 39, pp. 1640–1649, Sept. 1991.

[22] R. E. Collin, *Antennas and Radiowave Propagation*. New York: McGraw-Hill, 1985.

[23] J. E. Hipp, "Soil electromagnetic parameters as functions of frequency, soil density, and soil moisture," *Proc. IEEE*, vol. 62, pp. 98–103, Jan. 1974.

[24] S. Vitebskiy and L. Carin, "Resonances of perfectly conducting wires and bodies of revolution buried in a lossy dispersive half-space," *IEEE Trans. Antennas Propagat.*, vol. 44, pp. 1575–1583, Dec. 1996.

Vicente Losada received the Licenciado and Doctor degrees in physics from the University of Seville, Seville, Spain, in 1992 and 1997, respectively.

He has been an Assistant Professor in the Department of Applied Physics I, University of Seville, since 1999. In 2002, he spent three months as a Visiting Scholar at École Polytechnique Fédérale de Lausanne, Lausanne, Switzerland. His current research interests are focused on the numerical and experimental study of the resonance, radiation, and scattering properties of planar metallic patches embedded in multilayered media.

Rafael R. Boix (M'96) received the Licenciado and Doctor degrees in physics from the University of Seville, Seville, Spain, in 1985 and 1990, respectively.

Since 1986, he has been with the Electronics and Electromagnetism Department, University of Seville, where he became an Associate Professor in 1994. During the summers of 1991 and 1992, he was a Visiting Scholar with the Electrical Engineering Department, University of California, Los Angeles. During the summer of 1996, he was a Visiting Scholar with the Electrical and Computer Engineering Department, Syracuse University, Syracuse, NY. His current research interest is focused on the numerical analysis of the effects of complex substrates on the performance of planar passive microwave circuits, planar antennas and scatterers, and frequency-selective surfaces.

Francisco Medina (M'90–SM'01) received the Licenciado and Doctor degrees in physics from the University of Seville, Seville, Spain, in 1982 and 1987, respectively.

Since 1983, he has been with the Electronics and Electromagnetism Department, University of Seville, where he became an Associate Professor in 1990. He is currently the Head of the Microwaves Group at the University of Seville. Between 1986 and 1987, he spent the academic year at the Laboratoire de Microondes of L'Enseeiht, Toulouse, France. His current research interests include the study of analytical and numerical methods for the analysis of planar circuits, antennas, and scatterers embedded in multilayered media, and the analysis of the influence of lossy, dispersive, and anisotropic materials on these structures.